IOP Publishing Inverse Problems
Inverse Problems 32 (2016) 114001 (15pp) doi:10.1088/0266-5611/32/11/114001

Material reconstruction for spectral computed tomography with detector response function

Jiulong Liu[1] **and Hao Gao**[2]

[1] Department of Mathematics, Shanghai Jiao Tong University, Shanghai 200240, People's Republic of China
[2] Department of Radiation Oncology, Duke University Medical Center, Durham NC 27708, USA

E-mail: hao.gao.2012@gmail.com

Received 16 December 2015, revised 19 August 2016
Accepted for publication 8 September 2016
Published 3 October 2016

Abstract

Different from conventional computed tomography (CT), spectral CT using energy-resolved photon-counting detectors is able to provide the unprecedented material compositions. However accurate spectral CT needs to account for the detector response function (DRF), which is often distorted by factors such as pulse pileup and charge-sharing. In this work, we propose material reconstruction methods for spectral CT with DRF. The simulation results suggest that the proposed methods reconstructed more accurate material compositions than the conventional method without DRF. Moreover, the proposed linearized method with linear data fidelity from spectral resampling had improved reconstruction quality from the nonlinear method directly based on nonlinear data fidelity.

Keywords: computed tomography, sparsity regularization, image reconstruction

(Some figures may appear in colour only in the online journal)

1. Introduction

When the x-ray photon passes through a subject, it carries the information of a line integral of attenuation coefficients along the photon trajectory. This so-called x-ray transform is the forward model for x-ray computed tomography (CT), an inverse problem to reconstruct internal mapping of attenuation coefficients where multiple source–detector pairs generate boundary measurements from various angular views around the subject [1]. The x-ray photon transport is essentially polyenergetic rather than monoenergetic. That is both x-ray photons

and attenuation coefficients have the spectral dependence. Thus the ideal forward model should be also polyenergetic. However, since the conventional CT detectors are charge-integrating with no spectral resolution, the CT inverse problem is often based on the monoenergetic forward model and equivalently reconstructs a spectrally-averaged attenuation image. As a result, the imaging quality can be significantly deteriorated, the so-called beam hardening artifact, when the imaging subject contains the material for which the modeling error using monoenergetic forward model is significant, such as the metal implant or the bony structure of a patient [2]. This can be addressed by the recent development in energy-resolved photon-counting detector. Equipped with the photon-counting detector, spectral CT provides the unprecedented possibility to simultaneously reconstruct a series of spectral images [3–10].

Spectral CT allows the use of polyenergetic forward model and therefore its image reconstruction should be more accurate than the conventional CT. More importantly, it potentially meets the clinical and industrial needs of energy-resolved CT images or particularly material compositions, such as spectral breast CT [11–13] and K-edge imaging [14, 15]. In terms of reconstruction algorithm for spectral CT, the material compositions can be reconstructed with two different methodologies: a two-step procedure with first the reconstruction of spectral images and then material decomposition from these spectral images to material compositions [7, 12, 16–22] or alternatively first material-specific sinogram decomposition and then material reconstruction [15, 23–25]; a one-step procedure that directly reconstructs the material compositions by incorporating the material-image model into the reconstruction [7, 26]. Ideally the latter is preferred for two reasons: first the direct material reconstruction can fully utilize the structural similarity among materials; second it avoids to reconstruct an overdetermined system of images for material decomposition since the number of energy bins, correspondingly the number of spectral images, is often more than the number of materials to be reconstructed. Various sparsity-based reconstruction methods have been developed with the energy-by-energy reconstruction such as dictionary learning [16], tight frame [12, 19] and bilateral filtration [20], and the joint reconstruction to utilize the structural similarity in the spectral dimension such as total variation (TV) [22], nonlocal TV [27], patch-based low-rank model [21], rank-and-sparsity decomposition model [7] and tensor rank-and-sparsity decomposition model [18].

However, without considering the detector response function (DRF), the reconstruction quality of spectral CT can be significantly reduced, particularly for the photon-counting detector with high count rate and high spatial resolution [28, 29]. The DRF refers to the recorded spectral distribution for a monoenergetic incident beam at the detector [15]. Ideally the DRF should be a Gaussian distribution centered at the incident energy with a small standard deviation. Practically the DRF is distorted by factors such as pulse pileup and charge-sharing, and thus needs to be experimentally calibrated [15, 30, 31]. The methods to deal with the data distortion can be mostly classified into two categories: data correction and data compensation [32]. The key idea for data correction methods is to recover the data from the distortion, which can be used in turn for reconstruction [33–35]. However, the data correction strategy suffers from the fundamental ill-posedness in practice: the number of energy intervals for measurements is much smaller than the number of energy intervals in order for accurately discretizing the DRF. In contrast, the data compensation directly reconstructs spectral images from distorted data using DRF [36–39]. In this work, we consider DRF-based material reconstruction, i.e., the direct reconstruction of material compositions instead of first reconstructing spectral images and then material compositions, as the image-to-material decomposition problem can be overdetermined and the separate image reconstruction can have degraded reconstruction quality.

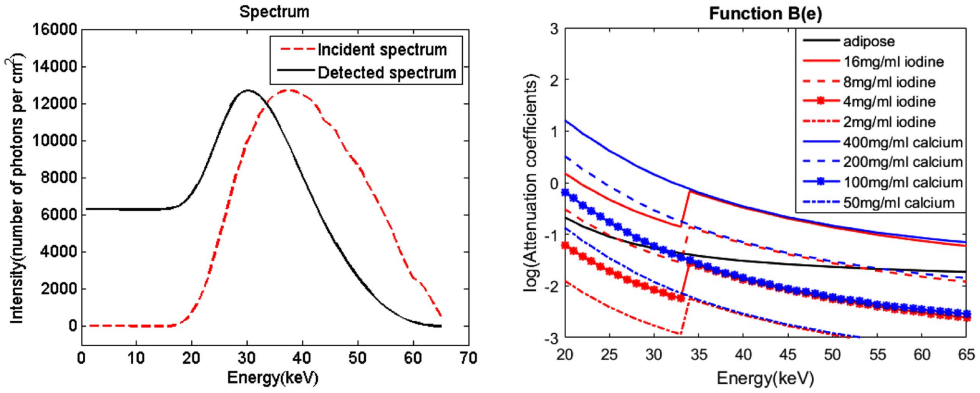

Figure 1. Left: the incident and detected spectrum with 65 keV tube voltage; right: material-attenuation function (log scale).

2. Method

2.1. Detector response function

For the purpose of accurate spectral CT, we consider the DRF to account for the detector response distortion due to factors such as pulse pileup and charge-sharing. Since the analytic determination of DRF is generally not available due to various complex physical processes, it is often estimated experimentally using monoenergetic photon spectra, such as synchrotron sources or radioactive isotopes [15, 30] or fluorescent characteristic emission [31]. Comparing with x-ray fluorescence, synchrotron sources may not be practically available and radioactive isotopes can be time-consuming or dangerous. Thus we adopt the DRF calibrated for a Silicon strip photon-counting detector using x-ray fluorescence. Here the Silicon detector is considered for its high spatial resolution and photon-counting rate. Note that although this specific DRF will be used throughout this work, the proposed method is generally applicable to other DRFs as well.

In this work, we adopt the following DRF calibrated using x-ray fluorescence [31]

$$D(E', E) = \begin{cases} c_1(E), & \text{for } E/2 < E' < E - 3\sigma; \\ \frac{c_2(E)}{\sqrt{2\pi}\,\sigma(E)} \exp\left(-\frac{(E'-E)^2}{2\sigma(E)^2}\right) + \frac{2c_3(E)}{\sqrt{2\pi}\,\sigma(E)} \int_{E'}^{\infty} \exp\left(-\frac{(E'-E)^2}{2\sigma(E)^2}\right) dE', & \text{for } E' > E - 3\sigma. \end{cases} \tag{1}$$

In (1), E denotes the incident photon energy at the detector, while E' is the received photon energy by the detector. Here the DRF is determined by four parameters that are experimentally calibrated: the standard deviation of the primary Gaussian peak $\sigma(E)$; three fitting parameters $c_1(E)$, $c_2(E)$ and $c_3(E)$ that are related to the fitted charge-sharing fractions [31]. This DRF models the energy response over the entire dynamic range and is reasonably accurate through experimental calibrations, where the energy dependence of the energy resolutions is characterized by the second-order polynomial and the least-square fitting is utilized for the charge-sharing fraction to account for the nonlinearity. For example, the fitted incident and detected spectrum with 65 keV tube voltage is plotted in the left image of figure 1.

2.2. Forward model

In this section, we give the polyenergetic x-ray forward model with DRF. For the discretization purpose, let us consider an incident spectrum $s(E)$ that consists of N_e intervals, i.e., $\{\Delta E_n,\ n = 1,\cdots,N_e\}$ with ΔE_n as the length of the nth energy interval, and a set of polyenergetic measurement $\{Y_{im},\ i = 1,\cdots,N_d,\ m = 1,\cdots,M_e\}$, where M_e is the number of energies at the detector, N_v the number of projection views, N_{d0} the number of detectors per view, and $N_d = N_{d0} \cdot N_v$. Let $M = N_d \cdot M_e$ be the total number of spectral data available for image reconstruction, $\Delta E'_m$ the length of the mth energy response interval at the detector, and L_i the path of line integral for Y_{im}. Here we assume the spectral measurement Y_{im} follows Poisson statistics with the expectation Y^*_{im}. With the above DRF (1) taken into account, the expectation Y^*_{im} obeys the following forward model

$$Y^*_{im} = \int_{\Delta E'_m} \mathrm{d}E' \sum_n \int_{\Delta E_n} D(E',\, E)S(E)\mathrm{e}^{-\int_{L_i} u(x,E)\mathrm{d}x}\mathrm{d}E. \tag{2}$$

Clearly many energy intervals (i.e., $\{\Delta E_n,\ n = 1,\cdots,N_e\}$) are needed for accurate discretization of the forward model (2), which implies the necessity of reconstructing a fair number of $u(x,\, E)$, i.e., N_e spectral images. However, the goal of spectral CT is to reconstruct the material compositions. To avoid such a redundant step of reconstructing an overdetermined system of $u(x,\, E)$, we utilize the linear dependence of $u(x,\, E)$ on material compositions Z to directly reconstruct Z, i.e.,

$$u(x,\, E) = \sum_{k=1}^{N_z} Z_k(x)B_k(E). \tag{3}$$

Here N_z is the number of basis materials, $Z_k(x)$ is the material composition of the kth basis material at the spatial location x, and $B_k(E)$ is the attenuation coefficient of the kth basis material at the energy E. Note that $Z_k(x)$ is spectrally independent, while $B_k(E)$ is spatially independent. As an example, the material-attenuation function $B(E)$ for several materials is plotted in the right image of figure 1.

Then let us consider the spatial discretization of (2) on a piecewise-constant spatial grid $\{x_j,\ j = 1,\cdots,N_x\}$. Let A be the system matrix for discretized x-ray transform with the matrix element A_{ij}, e.g., the length of the ray L_i overlapping with the grid x_j. Then our forward model with DRF for the direct reconstruction of material compositions is

$$Y^*_{im} = \int_{\Delta E'_m} \mathrm{d}E' \sum_n \int_{\Delta E_n} D(E',\, E)S(E)\mathrm{e}^{-\sum_j A_{ij}\left(\sum_k Z_{jk}B_k(E)\right)}\mathrm{d}E, \tag{4}$$

where Z_{jk} is the kth material composition at the grid x_j.

Next we introduce the effective attenuation coefficient B_{kn} of the kth basis material for the energy interval ΔE_n with respect to the incident spectrum, i.e.,

$$Y^*_{im} = \sum_n \mathrm{e}^{-\sum_j A_{ij}\left(\sum_k Z_{jk}B_{kn}\right)}R_{nm}, \tag{5}$$

with

$$R_{nm} = \int_{\Delta E'_m} \mathrm{d}E' \int_{\Delta E_n} D(E',\, E)S(E)\mathrm{d}E. \tag{6}$$

Here (5) is justified by the mean value theorem for definite integrals, thanks to the continuity of $B(E)$ with respect to E.

In the matrix notation, (5) is

$$Y^* = \mathrm{e}^{-AZB}R. \tag{7}$$

In (7), $A \in \mathbb{R}^{N_d \times N_x}$ is the system matrix, $Z \in \mathbb{R}^{N_x \times N_z}$ the material composition, $B \in \mathbb{R}^{N_z \times N_e}$ the material-attenuation matrix, $R \in \mathbb{R}^{N_e \times M_e}$ the energy response matrix, and $Y^* \in \mathbb{R}^{N_d \times M_e}$ the spectral measurement. Note that we unfold Y and Z to column vectors as needed in the following.

Finally, our polyenergetic x-ray forward model with DRF for given spectral CT data Y obeying the Poisson distribution is based on the following maximum likelihood function

$$p(Y|Z) = \prod_{i,m} \frac{(Y^*_{im})^{Y_{im}}}{Y_{im}!}\mathrm{e}^{-Y^*_{im}}, \tag{8}$$

and particularly its logarithmic version

$$\begin{aligned} L(Z) &= -\mathbf{ln}(p(Y|Z)) \\ &= -\sum_{i,m}(Y_{im}\mathbf{ln}([\mathrm{e}^{-AZB}R]_{im}) - [\mathrm{e}^{-AZB}R]_{im}), \end{aligned} \tag{9}$$

where $[\cdot]_{im}$ denotes the matrix element and $\mathbf{ln}(Y_{im}!)$ is ignored since it does not affect the optimization.

2.3. Material reconstruction with nonlinear data fidelity

We first consider the material reconstruction with nonlinear data fidelity (9), i.e.,

$$Z = \arg\min_Z L(Z) + \lambda|\nabla Z|_1, \tag{10}$$

where we use the isotropic TV term [40] for image regularization with a nonnegative regularization parameter λ, e.g., 2D isotropic TV term

$$|\nabla Z|_1 = \sqrt{(\partial_x Z)^2 + (\partial_y Z)^2}. \tag{11}$$

Although the main purpose of this paper is to study material reconstruction for spectral CT with DRF rather than the sparsity regularization, other choices of sparsity transform may improve the result, such as tensor framelet as a generalized isotropic TV norm [12, 19, 41–43] or low-rank models [7, 18, 21, 44, 45].

Note that the minimization problem is convex since both $|\nabla Z|_1$ and nonlinear data fidelity term are convex. The convexity of nonlinear data fidelity (9) essentially follows from the convexity of Poisson distribution [46]. It can also be directly verified as shown in the appendix.

2.4. Material reconstruction with linear data fidelity

Despite the convexity of nonlinear data fidelity based material reconstruction (10), its reconstruction quality may suffer from the nonlinearity. Alternatively we consider the following linear data fidelity based material reconstruction. Here the essential idea is to collaboratively resample incident energy intervals and detected energy intervals so that $R \in \mathbb{R}^{N_e \times M_e}$ is invertible with optimized condition number. Thus $N_e = M_e$.

Note that there are two spectral discretizations: one is with respect to spectral data, i.e., the number of rows of R indexed by m in (2); the other is with respect to DRF, i.e., the number of columns of R indexed by n in (2). Here n needs to be large enough in order to accurately represent DRF, assuming equal spectral partitions. Therefore, n is often larger than

m, and thus R is non-invertible. In the following, we shall optimize the spectral partitions so that R can be resampled as an invertible matrix without losing its accuracy for representing DRF.

A heuristically robust method is to first group the incident energy intervals ΔE_n using $S(E)$ to achieve the equal weighting, i.e.,

$$\int_{\Delta E_n} s(E)\mathrm{d}E = \frac{1}{M_e}\sum_n \int_{\Delta E_n} s(E)\mathrm{d}E. \tag{12}$$

and then group the detected energy intervals $\Delta E'_m$ using $D(E', E)S(E)$ to also achieve the equal weighting, i.e.,

$$\int_{\Delta E'_m} \mathrm{d}E' \sum_n \int_{\Delta E_n} D(E', E)s(E)\mathrm{d}E = \frac{1}{M_e}\sum_m \int_{\Delta E'_m} \mathrm{d}E' \sum_n \int_{\Delta E_n} D(E', E)s(E)\mathrm{d}E. \tag{13}$$

In this work, we adopt the heuristic method (12) and (13) and it works well with the aforementioned DRF (1). Note that R is now invertible after resampling, while it is not invertible originally in (7). Thus instead of the previous nonlinear data fidelity based material reconstruction (10), we have the following linear data fidelity based material reconstruction from (7)

$$Z^* = \arg\min_Z \|AZB - P\|_F^2 + \lambda|\nabla Z|_1, \tag{14}$$

where $P = -\mathbf{ln}(YR^{-1}) \in \mathbb{R}^{N_d \times M_e}$ and $\|\cdot\|_F$ is matrix Frobenius norm.

2.5. Material-attenuation matrix

Here we consider how to determine the material-attenuation matrix B_{kn} in (5).

Assuming Z is known for the calibration purpose, we can compute B by solving the following overdetermined nonlinear system (15)

$$e^{-AZB}R = Y. \tag{15}$$

Alternatively, without assuming Z is known, we rewrite (5) as

$$\begin{aligned}&\int_{\Delta E'_m} \mathrm{d}E' \sum_n \int_{\Delta E_n} D(E', E)S(E)\mathrm{e}^{-\sum_j A_{ij}\left(\sum_k Z_{jk}B_k(E)\right)}\mathrm{d}E\\ &= \sum_n \mathrm{e}^{-\sum_j A_{ij}\left(\sum_k Z_{jk}B_{kn}\right)} \int_{\Delta E'_m} \mathrm{d}E' \int_{\Delta E_n} D(E', E)S(E)\mathrm{d}E.\end{aligned} \tag{16}$$

Now considering the ray passing through the center of a unit circular/spherical domain of the kth material only, (16) is reduced to the following overdetermined nonlinear system

$$\begin{aligned}&\int_{\Delta E'_m} \mathrm{d}E' \sum_n \int_{\Delta E_n} D(E', E)S(E)\mathrm{e}^{-B_k(E)}\mathrm{d}E\\ &= \sum_n \mathrm{e}^{-B_{kn}} \int_{\Delta E'_m} \mathrm{d}E' \int_{\Delta E_n} D(E', E)S(E)\mathrm{d}E.\end{aligned} \tag{17}$$

On the other hand, when using the linearized data fidelity model (14), when Z is known, similar to (15), we can simply solve the following overdetermined linear system (18)

$$AZB = P. \tag{18}$$

When Z is unknown,similar to (17), we can solve the following full-rank linear system (19)

$$B_{kn} = -[\mathbf{ln}(Y^k R^{-1})]_n. \tag{19}$$

where $Y^k \in \mathbb{R}^{M_e}$ with $[Y^k]_m = \int_{\Delta E'_m} \mathrm{d}E' \sum_n \int_{\Delta E_n} D(E', E) S(E) \mathrm{e}^{-B_k(E)} \mathrm{d}E$.

In this work, given the material-attenuation function $B(E)$ (e.g., the right image of figure 1), the material-attenuation matrix B is computed by (17) or (19).

2.6. Solution algorithm

The solution algorithm for sparsity-based reconstruction problems (10) and (14) can be based on alternating direction method of multipliers [47] or split Bregman method [48]. Here we give the details for solving (10) and (14).

In order to solve the L1-type problems (10) and (14) with non-differentiable L1 norm, we introduce a dummy variable $d = \nabla Z$ to decouple the sparsity regularization from the data fidelity, i.e.,

$$\min_{(Z,c)} L(Z) + \lambda |c|_1 \quad s.t. \quad c = \nabla Z. \tag{20}$$

Then the augmented Lagrangian of (20) is

$$J(Z, c, b) = L(Z) + \tfrac{\rho}{2} \|\nabla Z - c + b\|_2^2 + \lambda |c|_1. \tag{21}$$

To obtain saddle points of the augmented Lagrangian (21) based on ADMM is to iteratively solve

$$\begin{cases} Z^{k+1} = \arg\min_Z J(Z, c^k, b^k), \\ c^{k+1} = \arg\min_c J(Z^{k+1}, c, b^k), \\ b^{k+1} = b^k + \nabla Z^{k+1} - c^{k+1}. \end{cases} \tag{22}$$

Note that the solution algorithm for either nonlinear or linear data fidelity is based on the ADMM loop (22). While the sparsity subproblem (c-subproblem) is the same, the data fidelity subproblem (Z-subproblem) is different. Next we provide the solution algorithm for the Z-subproblem in (22) with nonlinear data fidelity (10) or linear data fidelity (14).

- For nonlinear data fidelity (10), we apply the nonlinear conjugate gradient method to generate the sequence $Z^{k,q}$, $q \geqslant 1$ with an initial guess Z^k as $Z^{k,0}$, i.e.

$$\begin{cases} Z^{k,q} = Z^{k,q} + \alpha^q d^q, \\ d^{q+1} = -g^{q+1} + \beta^q d^q. \end{cases} \tag{23}$$

  where the positive step size α^q is obtained by a line search and g^{q+1} is

$$g^{q+1} = \nabla L(Z^{k,q}) + \rho \nabla^T (\nabla Z - c^k + b^k) \tag{24}$$

  with $\nabla L(Z^{k,q})$ computed using (31) and the update parameter β^q is given by

$$\beta^q = \frac{(g^{q+1})^\mathsf{T} \nabla_Z^2 J(Z^{k,q}, c^k, b^k) d^q}{(d^q)^\mathsf{T} \nabla_Z^2 J(Z^{k,q}, c^k, b^k) d^q}, \tag{25}$$

  where $\nabla_Z^2 J(Z^{k,q}, c^k, b^k)$ is the Hessian matrix given by

$$\nabla_Z^2 J(Z^{k,q}, c^k, b^k) = \nabla^2 L(Z^{k,q}) + \rho \nabla^\mathsf{T} \nabla \tag{26}$$

with $\nabla^2 L(Z^{k,q})$ computed using (32). Last, we update Z^{k+1} using the final inner-loop solution $Z^{k,q}$.

- For linear data fidelity (14), the optimal condition for the first subproblem in (22) provides

$$A^{\mathsf{T}}(AZB - P)B^{\mathsf{T}} + \rho\nabla^{\mathsf{T}}(\nabla Z - c^k + b^k) = 0. \tag{27}$$

The equation (27) is a linear system that can be efficiently solved by standard conjugate gradient method (see [49] for example).

The vector d^{k+1} in the second subproblem in (22) can be analytically solved by applying the following isotropic soft-shrinkage formula pointwisely

$$\begin{cases} c_x^{k+1} = \dfrac{\partial_x Z^k + b_x^k}{\sqrt{(\partial_x Z^k + b_x^k)^2 + (\partial_y Z^k + b_y^k)^2}} \cdot \max\left(\sqrt{(\partial_x Z^k + b_x^k)^2 + (\partial_y Z^k + b_y^k)^2} - \dfrac{\lambda}{\rho}, 0\right), \\ c_y^{k+1} = \dfrac{\partial_y Z^k + b_y^k}{\sqrt{(\partial_x Z^k + b_x^k)^2 + (\partial_y Z^k + b_y^k)^2}} \cdot \max\left(\sqrt{(\partial_x Z^k + b_x^k)^2 + (\partial_y Z^k + b_y^k)^2} - \dfrac{\lambda}{\rho}, 0\right). \end{cases} \tag{28}$$

For the convenience of implementation, the solution algorithm for nonlinear data fidelity (10) or linear data fidelity (14) is summarized as follows.

Algorithm 1. Material reconstruction with nonlinear data fidelity.

$Z^0 = \mathbf{0}$, $k = 0$
while $\|Z^{K+1} - Z^K\|_2 > \delta_1$ **do**
  $Z^{k,0} = Z^k$, $g^0 = \nabla L(Z^{k,0}) + \rho\nabla^{\mathsf{T}}(\nabla Z^{k,0} - c^k + f^k)$, $d^0 = -g^0$, $q = 0$
  while $\|g^q\|_2 > \delta_2$ **do**
    α^q by line search
    $Z^{k,q} = Z^{k,q} + \alpha^q d^q$
    $g^{q+1} = \nabla L(Z^{k,q}) + \rho\nabla^{\mathsf{T}}(\nabla Z^{k,q} - c^k + b^k)$
    $\beta^q = \frac{(g^{q+1})^{\mathsf{T}}(\nabla^2 L(Z^{k,q}) + \rho\nabla^{\mathsf{T}}\nabla)d^q}{(d^q)^{\mathsf{T}}(\nabla^2 L(Z^{k,q}) + \rho\nabla^{\mathsf{T}}\nabla)d^q}$
    $d^{q+1} = -g^{q+1} + \beta^q d^q$
    $q = q + 1$
  end while
  $Z^{k+1} = Z^{k,q}$
  $c_x^{k+1} = \dfrac{\partial_x Z^k + b_x^k}{\sqrt{(\partial_x Z^k + b_x^k)^2 + (\partial_y Z^k + b_y^k)^2}} \cdot \max\left(\sqrt{(\partial_x Z^k + b_x^k)^2 + (\partial_y Z^k + b_y^k)^2} - \dfrac{\lambda}{\rho}, 0\right)$
  $c_y^{k+1} = \dfrac{\partial_y Z^k + b_y^k}{\sqrt{(\partial_x Z^k + b_x^k)^2 + (\partial_y Z^k + b_y^k)^2}} \cdot \max\left(\sqrt{(\partial_x Z^k + b_x^k)^2 + (\partial_y Z^k + b_y^k)^2} - \dfrac{\lambda}{\rho}, 0\right)$
  $b_x^{k+1} = b_x^k + (\partial_x Z^{k+1} - c_x^{k+1})$
  $b_y^{k+1} = b_y^k + (\partial_y Z^{k+1} - c_y^{k+1})$
  $k = k + 1$
end while

Algorithm 2. Material reconstruction algorithm with linear data fidelity.

$Z^0 = \mathbf{0}$, $k = 0$
while $\|Z^{K+1} - Z^K\|_2 > \delta_1$ **do**
  $Z^{k,0} = Z^k$, $g^0 = A^{\mathsf{T}}W(AZ^{k,0}B - P)B^{\mathsf{T}} + \rho\nabla^{\mathsf{T}}(\nabla Z^{k,0} - c^k + f^k)$, $d^0 = -g^0$, $s^0 = (g^0)^{\mathsf{T}}g^0$, $q = 0$
  while $\|g^q\|_2 > \delta_2$,**do**
    $H^q = A^{\mathsf{T}}WAZ^{k,q}BB^{\mathsf{T}} + \rho\nabla^{\mathsf{T}}\nabla Z^{k,q}$

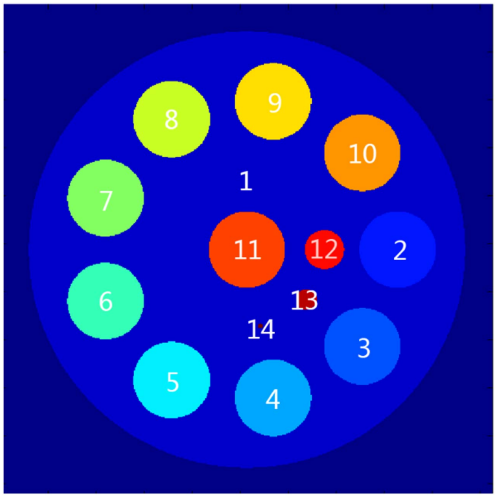

Figure 2. The simulation phantom.

(Continued.)

$\alpha^q = \frac{s^q}{(d^q)^T H^q}$
$Z^{k,q} = Z^{k,q} + \alpha^q d^q$
$g^{q+1} = g^k + \alpha H$
$s^{k+1} = (g^{q+1})^T g^{q+1}$
$\beta^q = \frac{s^{q+1}}{s^q}$
$d^{q+1} = -g^{q+1} + \beta^q d^q$
$q = q + 1$
end while
$Z^{k+1} = Z^{k,q}$
$c_x^{k+1} = \frac{\partial_x Z^k + b_x^k}{\sqrt{(\partial_x Z^k + b_x^k)^2 + (\partial_y Z^k + b_y^k)^2}} \cdot \max\left(\sqrt{(\partial_x Z^k + b_x^k)^2 + (\partial_y Z^k + b_y^k)^2} - \frac{\lambda}{\rho}, 0\right)$
$c_y^{k+1} = \frac{\partial_y Z^k + b_y^k}{\sqrt{(\partial_x Z^k + b_x^k)^2 + (\partial_y Z^k + b_y^k)^2}} \cdot \max\left(\sqrt{(\partial_x Z^k + b_x^k)^2 + (\partial_y Z^k + b_y^k)^2} - \frac{\lambda}{\rho}, 0\right)$
$b_x^{k+1} = b_x^k + (\partial_x Z^{k+1} - c_x^{k+1})$
$b_y^{k+1} = b_y^k + (\partial_y Z^{k+1} - c_y^{k+1})$
$k = k + 1$
end while

3. Results

Simulations were performed at tube voltage of 65 kVp. The mean glandular dose was estimated to be approximately 2 mGy for a 10 cm breast with 40% density. A 10 cm PMMA phantom (figure 2) which contains both iodine and calcium of various concentrations (table 1) was used. The simulation environment was MATLAB R2013b using NVIDIA Tesla K80 GPU. The x-ray transform and its adjoint (computationally dominant components) were

Table 1. The concentration and size of phantom objects.

Object	Material	Radius	Concentration
1	Adipose	48 mm	
2	Iodine	8 mm	16 mg ml^{-1}
3, 10	Iodine	8 mm	8 mg ml^{-1}
4	Iodine	8 mm	4 mg ml^{-1}
5, 11	Iodine	8 mm	2 mg ml^{-1}
6	Calcium	8 mm	400 mg ml^{-1}
7, 10	Calcium	8 mm	200 mg ml^{-1}
8	Calcium	8 mm	100 mg ml^{-1}
9,11	Calcium	8 mm	50 mg ml^{-1}
12	Calcium	4 mm	400 mg ml^{-1}
13	Calcium	2 mm	400 mg ml^{-1}
14	Calcium	0.6 mm	400 mg ml^{-1}

Table 2. Energy bins($\Delta E_m = (E_{m-1}, E_m)$, $\Delta E'_m = (E'_{m-1}, E'_m)$).

m	0	1	2	3	4	5	6	7	8	9	10	11	12	13	14	15
E_m	1	22	25	27	29	31	33	35	37	39	42	45	47	51	55	65
E'_m	1	20	23	25	27	29	31	33	35	37	39	42	44	39	48	52

computed on-the-fly in parallel on GPU [50], while the rest was computed on CPU. The total computational time was less than twenty minutes for each nonlinear data fidelity based material reconstruction and less than ten minutes for each linear data fidelity based material reconstruction.

To mimic the generation of projection data in practice, we obtained 66 measurements linearly with respect to the energy with 1 keV gap, i.e.,

$$Y^*_{m'} = \sum_{n=1}^{65} \mathrm{e}^{-AZB_n} R(n,\, m'), \text{ for } m' = 1, \cdots, 65, \tag{29}$$

where AZB was computed with 600 views and 768 detectors per view and with total exposure of 1200mR for each energy scan.

Then, we divided the energy $1 \leqslant \tilde{E} \leqslant 65$ into fifteen energy groups (table 2).

Then we added the Poisson noise to the measurements from each energy bin, i.e.,

$$Y_m = \mathbf{Possionrnd}\left(\sum_{m' \in \Delta E'_m} Y_{m'} \right), \quad \text{for } m = 1, \cdots, 15, \tag{30}$$

where $\mathbf{Possionrnd}(\lambda)$ returns random numbers generated by the Poisson distribution with the parameter λ.

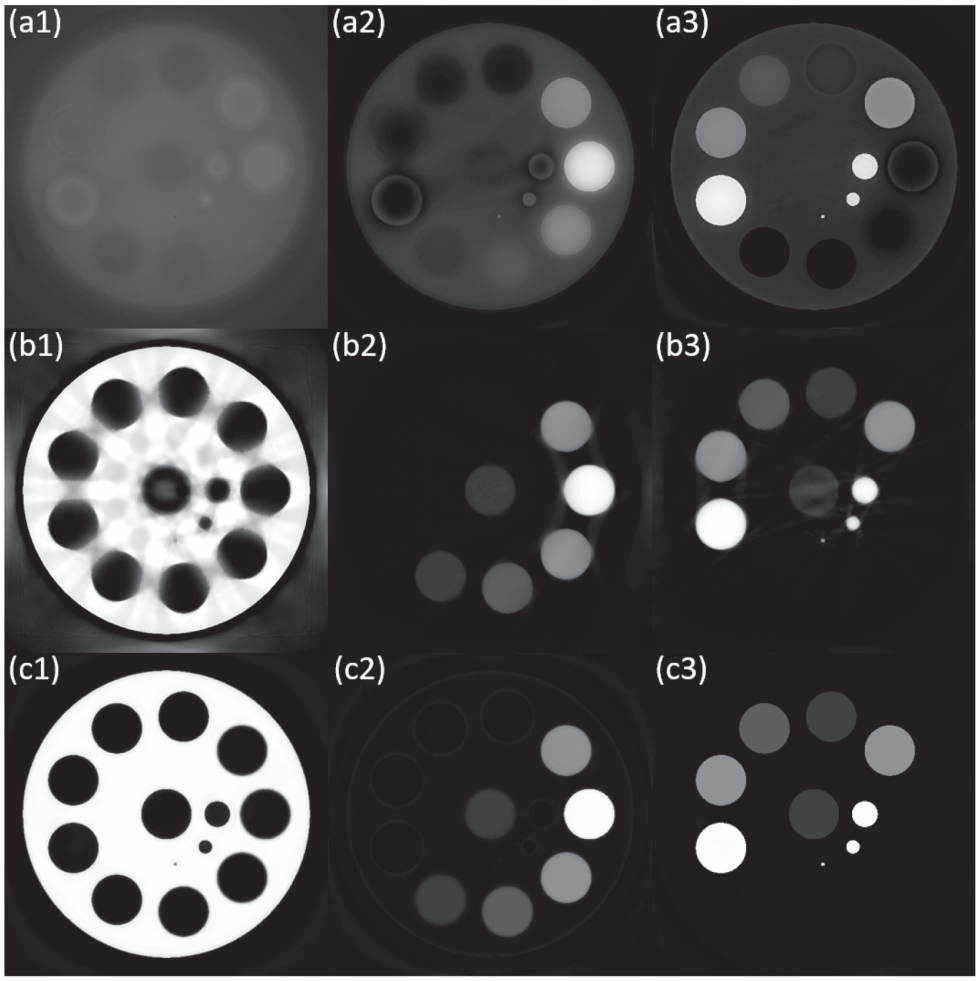

Figure 3. Simulation results. (a) standard material reconstruction method without DRF; (b) the proposed method with DRF and nonlinear data fidelity; (c) the proposed method with DRF and linear data fidelity. (1) adipose; (2) iodine; (3) calcium.

To compare with the proposed material reconstruction methods with DRF (10) and (14), we considered standard material reconstruction method without DRF [27], which has the same formulation as (9) except that the DRF $D(E', E)$ does not appear in the data fidelity term (2) and can be solved similarly by the ADMM algorithm (22) with a distinct data fidelity step.

The reconstructed material composition images with simulated data are shown in figure 3. Our proposed material reconstruction methods with DRF (10) and (14) were able to accurately reconstruct the phantom material compositions into adipose, iodine and calcium basis while the standard method failed to do so. Moreover, the reconstruction quality with linear data fidelity (14) is better than that with nonlinear data fidelity (10). Note that the problem under consideration is nonlinear due to DRF. Since the problem is nonlinear,

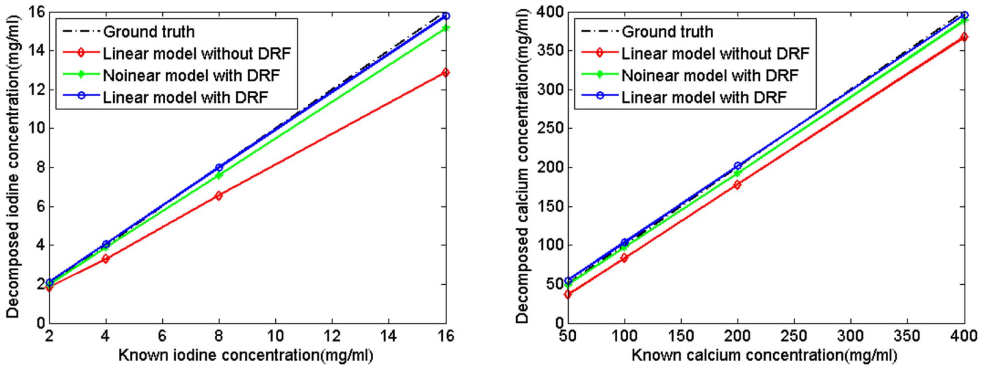

Figure 4. Left: material concentration of iodine (object 2–5); right: material concentration of calcium (object 6–9).

although the nonlinear data fidelity based method here did not achieve satisfactory reconstruction quality, better solution algorithm may be available.

The mean material concentration is plotted in figure 4, which again shows that the proposed methods with DRF provided accurate material compositions.

4. Conclusion

We have proposed material reconstruction methods for spectral CT with DRF, which provided more accurate material compositions than the standard methods without DRF. Moreover, the proposed method with linear data fidelity had improved reconstruction quality from the proposed method with nonlinear data fidelity.

Acknowledgments

The authors are grateful to the reviewers for their valuable comments. The authors thank Dr Huanjun Ding with University of California at Irvine for providing experimentally calibrated DRF and the inspiring discussion.

Appendix

Lemma 1. *The nonlinear data fidelity* L(Z) *(9) is a convex function.*

Proof 1. let us first consider the first-order gradient of $L(Z)$ (9) with respect to $Z_{j'k'}$ is

$$\begin{aligned}\frac{\partial L(Z)}{\partial Z_{j'k'}} &= -\sum_{i,m}\left(\frac{\partial\left(Y_{im}\ln\left(\sum_n e^{-\sum_j A_{ij}\left(\sum_k Z_{jk}B_{kn}\right)}R_{nm}\right)\right)}{\partial Z_{j'k'}} - \frac{\partial\left(\sum_n e^{-\sum_j A_{ij}\left(\sum_k Z_{jk}B_{kn}\right)}R_{nm}\right)}{\partial Z_{j'k'}}\right),\\ &= \sum_{i,m} Y_{im}\frac{A_{ij'}\sum_n e^{-\sum_j A_{ij}\left(\sum_k Z_{jk}B_{kn}\right)}B_{k'n}R_{nm}}{\sum_n e^{-\sum_j A_{ij}\left(\sum_k Z_{jk}B_{kn}\right)}R_{nm}} - \sum_{i,m}A_{ij'}\sum_n e^{-\sum_j A_{ij}\left(\sum_k Z_{jk}B_{kn}\right)}B_{k'n}R_{nm}.\end{aligned} \tag{31}$$

Then we consider the second-order gradient of $L(Z)$ (9), i.e.,

$$\begin{aligned}\frac{\partial^2 L(Z)}{\partial Z_{j'k'}\partial Z_{j''k''}} &= \sum_{i,m}\frac{\partial\left(Y_{im}\frac{A_{ij'}\sum_n \mathrm{e}^{-\sum_j A_{ij}\left(\sum_k Z_{jk}B_{kn}\right)}B_{k'n}R_{nm}}{\sum_n \mathrm{e}^{-\sum_j A_{ij}\left(\sum_k Z_{jk}B_{kn}\right)}R_{nm)}}\right)}{\partial Z_{j''k''}} - \sum_{i,m}\frac{\partial(A_{ij'}\sum_n \mathrm{e}^{-\sum_j A_{ij}\left(\sum_k Z_{jk}B_{kn}\right)}B_{k'n}R_{nm})}{\partial Z_{j''k''}},\\ &= \sum_{i,m}Y_{im}\frac{-A_{ij'}A_{ij''}\left(\sum_n \mathrm{e}^{-\sum_j A_{ij}\left(\sum_k Z_{jk}B_{kn}\right)}B_{k'n}B_{k''n}R_{nm}\right)\left(\sum_n \mathrm{e}^{-\sum_j A_{ij}\left(\sum_k Z_{jk}B_{kn}\right)}R_{nm}\right)}{\left(\sum_n \mathrm{e}^{-\sum_j A_{ij}\left(\sum_k Z_{jk}B_{kn}\right)}R_{nm}\right)^2}\\ &\quad - \sum_{i,m}Y_{im}\frac{(A_{ij'}\left(\sum_n \mathrm{e}^{-\sum_j A_{ij}\left(\sum_k Z_{jk}B_{kn}\right)}B_{k'n}R_{nm}\right)\left(-A_{ij''}\sum_n \mathrm{e}^{-\sum_j A_{ij}\left(\sum_k Z_{jk}B_{kn}\right)}B_{k''n}R_{nm}\right)}{\left(\sum_n \mathrm{e}^{-\sum_j A_{ij}\left(\sum_k Z_{jk}B_{kn}\right)}R_{nm}\right)^2}\\ &\quad + \sum_{i,m}A_{ij'}A_{ij''}\sum_n \mathrm{e}^{-\sum_j A_{ij}\left(\sum_k Z_{jk}B_{kn}\right)}B_{k'n}B_{k''n}R_{nm},\\ &= \sum_{i,m}A_{ij'}A_{ij''}\sum_n \mathrm{e}^{-\sum_j A_{ij}\left(\sum_k Z_{jk}B_{kn}\right)}R_{nm}B_{k'n}B_{k''n}.\end{aligned} \tag{32}$$

Thus,

$$\begin{aligned}&\sum_{j'k'}Z_{j'k'}\sum_{j''k''}Z_{j''k''}\frac{\partial^2 L(Z)}{\partial Z_{j'k'}\partial Z_{j''k''}}\\ &\quad=\sum_{i,m}\sum_n \mathrm{e}^{-\sum_j A_{ij}(\sum_k Z_{jk}B_{kn})}R_{nm}\left(\sum_{j'k'}Z_{j'k'}A_{ij'}B_{k'n}\right)^2 \geqslant 0.\end{aligned} \tag{33}$$

Since the Hessian matrix (32) is positive semidefinite for $Z \in \mathbb{R}^{N_x \times N_z}$, $L(Z)$ is convex.

References

[1] Natterer F 1986 *The Mathematics of Computerized Tomography* vol 32 (Philadelphia: SIAM)

[2] Buzug T M 2008 *Computed Tomography: from Photon Statistics to Modern Cone-Beam CT* (Berlin: Springer)

[3] Fralliciardi P M, Jakubek J, Vavrik D and Dammer J 2009 Comparison of single-photon counting and charge-integrating detectors for x-ray high-resolution imaging of small biological objects *Nucl. Instrum. Methods Phys. Res.* A **607** 221–2

[4] Taguchi K, Srivastava S, Kudo H and Barber W C 2009 Enabling photon counting clinical x-ray CT *In Nuclear Science Symposium Conference Record (NSS/MIC)* vol 2009, pp 3581–5

[5] Bornefalk H and Danielsson M 2010 Photon-counting spectral computed tomography using silicon strip detectors: a feasibility study *Phys. Med. Biol.* **55** 1999–2022

[6] Cormode D P *et al* 2010 Atherosclerotic plaque composition: analysis with multicolor CT and targeted gold nanoparticles1 *Radiology* **3** 774–82

[7] Gao H, Yu H, Osher S and Wang G 2011 Multi-energy CT based on a prior rank, intensity and sparsity model (PRISM) *Inverse Problems* **27** 115012

[8] Shikhaliev P M and Fritz S G 2011 Photon counting spectral CT versus conventional CT: comparative evaluation for breast imaging application *Phys. Med. Biol.* **56** 1905

[9] Wang X, Meier D, Mikkelsen S, Maehlum G E, Wagenaar D J, Tsui B M, Patt B E and Frey E C 2011 MicroCT with energy-resolved photon-counting detectors *Phys. Med. Biol.* **56** 2791

[10] Ding H, Ducote J L and Molloi S 2012 Breast composition measurement with a cadmium–zinc–telluride based spectral computed tomography system *Med. Phys.* **39** 1289–97

[11] Ding H, Klopfer M J, Ducote J L, Masaki F and Molloi S 2014 Breast tissue characterization with photon-counting spectral CT imaging: a postmortem breast study *Radiology* **272** 731–8

[12] Ding H, Gao H, Zhao B, Cho H M and Molloi S 2014 A high-resolution photon-counting breast CT system with tensor-framelet based iterative image reconstruction for radiation dose reduction *Phys. Med. Biol.* **59** 6005
[13] Kalender W A, Beister M, Boone J M, Kolditz D, Vollmar S V and Weigel M C C 2012 High-resolution spiral CT of the breast at very low dose: concept and feasibility considerations *Eur. Radiol.* **22** 1–8
[14] Bornefalk H and Danielsson M 2010 Photon-counting spectral computed tomography using silicon strip detectors: a feasibility study *Phys. Med. Biol.* **55** 1999–2022
[15] Roessl E and Proksa R 2007 K-edge imaging in x-ray computed tomography using multi-bin photon counting detectors *Phys. Med. Biol.* **52** 4679–96
[16] Zhao B, Ding H, Lu Y, Wang G, Zhao J and Molloi S 2012 Dual-dictionary learning-based iterative image reconstruction for spectral computed tomography application *Phys. Med. Biol.* **57** 8217
[17] Zhao B, Ding H, Lu Y, Wang G, Zhao J and Molloi S 2012 Dual-dictionary learning-based iterative image reconstruction for spectral computed tomography application *Phys. Med. Biol.* **57** 8217
[18] Li L, Chen Z, Wang G, Chu J and Gao H 2013 A tensor PRISM algorithm for multi-energy CT reconstruction and comparative studies *J. X-Ray Sci. Technol.* **2** 147–63
[19] Zhao B, Gao H, Ding H and Molloi S 2013 Tight-frame based iterative image reconstruction for spectral breast CT *Med. Phys.* **40** 031905
[20] Clark D P and Badea C T 2014 Spectral diffusion: an algorithm for robust material decomposition of spectral CT data *Phys. Med. Biol.* **59** 6445
[21] Kim K, Ye J C, Worstell W, Ouyang J, Rakvongthai Y, Fakhri G E and Quanzheng L 2015 Sparse-view spectral CT reconstruction using spectral patch-based low-rank penalty *IEEE Trans. Med. Imaging* **34** 748–60
[22] Shen L and Xing Y 2015 Multienergy CT acquisition and reconstruction with a stepped tube potential scan *Med. Phys.* **42** 282–96
[23] Alvarez R E and Macovski A 1976 Energy-selective reconstructions in x-ray computerized tomography *Phys. Med. Biol.* **21** 733–44
[24] Schirra C O, Roessl E, Koehler T, Brendel B, Thran A, Pan D, Anastasio M A and Proksa R 2013 Statistical reconstruction of material decomposed data in spectral CT *IEEE Trans. Med. Imaging* **32** 1249–57
[25] Xu Q, Sawatzky A, Anastasio M A and Schirra C O 2014 Sparsity-regularized image reconstruction of decomposed K-edge data in spectral CT *Phys. Med. Biol.* **59** N65
[26] Long Y and Fessler J A 2014 Multi-material decomposition using statistical image reconstruction for spectral CT *IEEE Trans. Med. Imaging* **33** 1614–26
[27] Liu J, Ding H, Molloi S, Zhang X and Gao H 2015 MO-FG-204-07: nonlocal total variation based spectral CT image reconstruction *Med. Phys.* **42** 3570–3570
[28] Wang A S, Harrison D, Lobastov V and Tkaczyk J E 2011 Pulse pileup statistics for energy discriminating photon counting x-ray detectors *Med. Phys.* **38** 4265–75
[29] Ding H and Molloi S 2012 Image-based spectral distortion correction for photon-counting x-ray detectors *Med. Phys.* **39** 1864–76
[30] Xu C, Chen H, Persson M, Karlsson S, Danielsson M, Svensson C and Bornefalk H 2013 Energy resolution of a segmented silicon strip detector for photon-counting spectral CT *Nucl. Instrum. Methods Phys. Res.* A **715** 11–7
[31] Ding H, Cho H M, Barber W C, Iwanczyk J S and Molloi S 2014 Characterization of energy response for photon-counting detectors using x-ray fluorescence *Med. Phys.* **41** 121902
[32] Taguchi K and Iwanczyk J S 2013 Vision 20/20: single photon counting x-ray detectors in medical imaging *Med. Phys.* **40** 100901
[33] Miyajima S, Imagawa K and Matsumoto M 2002 CdZnTe detector in diagnostic x-ray spectroscopy *Med. Phys.* **29** 1421–9
[34] Kappler S, Hoelzer S, Kraft E, Stierstorfer K and Flohr T G 2011 Quantum-counting CT in the regime of count-rate paralysis: introduction of the pile-up trigger method *Proc. SPIE* **7961** 79610T
[35] Kraft E, Glasser F, Kappler S, Niederloehner D and Villard P 2012 Experimental evaluation of the pile-up trigger method in a revised quantumcounting CT detector *Proc. SPIE* **8313** 83134A
[36] Schlomka J P *et al* 2008 Experimental feasibility of multi-energy photon-counting Kedge imaging in pre-clinical computed tomography *Phys. Med. Biol.* **53** 4031–47

[37] Roessl E, Brendel B, Engel K, Schlomka J, Thran A and Proksa R 2011 Sensitivity of photon-counting based K-edge imaging in x-ray computed tomography *IEEE Trans. Med. Imaging* **30** 1678–90
[38] Srivastava S, Cammin J, Fung G S K, Tsui B M W and Taguchi K 2012 Spectral response compensation for photon-counting clinical x-ray CT using sinogram restoration *Proc. SPIE* **8315** 8315–37
[39] Srivastava S and Taguchi K 2010 Sinogram restoration algorithm for photon counting clinical x-ray CT with pulse pileup compensation *Proc. 1st Int. Meeting on Image Formation in X-Ray Computed Tomography (Salt Lake City, UT 59)*
[40] Rudin L I, Osher S and Fatemi E 1992 Nonlinear total variation based noise removal algorithms *Physica* D **60** 259–68
[41] Gao H, Li R, Lin Y and Xing L 2012 4D cone beam CT via spatiotemporal tensor framelet *Med. Phys.* **39** 6943–6
[42] Gao H, Qi X S, Gao Y and Low D A 2013 Megavoltage CT imaging quality improvement on TomoTherapy via tensor framelet *Med. Phys.* **40** 081919
[43] Zhou W, Cai J-F and Gao H 2013 Adaptive tight frame based medical image reconstruction: a proof-of-concept study for computed tomography *Inverse Problems* **29** 125006
[44] Gao H, Cai J-F, Shen Z and Zhao H 2011 Robust principal component analysis-based four-dimensional computed tomography *Phys. Med. Biol.* **56** 3181–98
[45] Cai J F, Jia X, Gao H, Jiang S B, Shen Z and Zhao H 2014 Cine cone beam CT reconstruction using low-rank matrix factorization: algorithm and a proof-of-principle study *IEEE Trans. Med. Imaging* **33** 1581–91
[46] Berenshtein A D, Vainshtein A D and Kreinin A Y 1989 A convexity property of the Poisson distribution and its application in queueing theory *J. Math. Sci.* **47** 2288–92
[47] Boyd S, Parikh N, Chu E, Peleato B and Eckstein J 2011 Distributed optimization and statistical learning via the alternating direction method of multipliers *Found. Trends Mach. Learn.* **3** 1–22
[48] Goldstein T and Osher S 2009 The split Bregman algorithm for l1 regularized problems *SIAM J. Imaging Sci.* **2** 323–43
[49] Nocedal J and Wright S J 2006 Conjugate gradient methods *Numerical Optimization* (Berlin: Springer) pp 101–34
[50] Gao H 2012 Fast parallel algorithms for the x-ray transform and its adjoint *Med. Phys.* **39** 7110–20